HHS Public Access

Author manuscript

Exp Neurol. Author manuscript; available in PMC 2021 April 01.

Published in final edited form as:

Exp Neurol. 2020 April ; 326: 113164. doi:10.1016/j.expneurol.2019.113164.

Neuronal ablation of mt-AspRS in mice induces immune pathway activation prior to severe and progressive cortical and behavioral disruption

Christina L Nemeth[1], **Sophia N Tomlinson**[1], **Melissa Rosen**[1], **Brett M O'Brien**[1], **Oscar Larraza**[1], **Mahim Jain**[1], **Connor F Murray**[1], **Joel S Marx**[1], **Michael Delannoy**[3], **Amena S Fine**[1,2], **Dan Wu**[4], **Aleksandra Trifunovic**[5], **Ali Fatemi**[1,6,*]

[1]Moser Center for Leukodystrophies, Kennedy Krieger Institute

[2]Department of Neurology and Developmental Medicine, Kennedy Krieger Institute, Baltimore, MD, USA

[3]Department of Cell Biology, Johns Hopkins University School of Medicine, Baltimore, MD, USA

[4]Department of Radiology and Radiological Science, Johns Hopkins University School of Medicine, Baltimore, MD, USA

[5]CECAD Research Centre, Institute for Mitochondrial Diseases and Aging, Center for Molecular Medicine Cologne, Medical Faculty, University of Cologne, Cologne, Germany

[6]Department of Neurology, Johns Hopkins University School of Medicine, Baltimore, MD, USA

Abstract

Leukoencephalopathy with brain stem and spinal cord involvement and lactate elevation (LBSL) is a rare, slowly progressive white matter disease caused by mutations in the mitochondrial aspartyl-tRNA synthetase (mt-AspRS, or DARS2). While patients show characteristic MRI T2 signal abnormalities throughout the cerebral white matter, brain stem, and spinal cord, the phenotypic spectrum is broad and a multitude of gene variants have been associated with the disease. Here, *Dars2* deletion from CamKIIα-expressing cortical and hippocampal neurons results in slowly progressive increases in behavioral activity at 5 months, and culminating by 9 months as severe brain atrophy, behavioral dysfunction, reduced corpus callosum thickness, and microglial morphology indicative of neuroinflammation. Interestingly, RNAseq based gene expression studies performed prior to the presentation of this severe phenotype reveal the upregulation of several pathways involved in immune activation, cytokine production and signaling, and the defense response regulation. RNA transcript analysis demonstrates that activation of immune and cell stress pathways are initiated in advance of a behavioral phenotype and cerebral deficits. An

[*]Corresponding Author: Ali Fatemi, MD, MBA, Kennedy Krieger Institute, 707 N Broadway, Baltimore, MD 21205, 443-923-2750, fatemi@kennedykrieger.org.

Declaration of interest: AF is a paid drug safety monitoring board member for Bluebird Bio, Stealth Biotherapeutics, and a paid consultant to Calico Labs.

understanding of these pathways and their contribution to significant neuronal loss in CamKII-*Dars2* KO mice may aid in deciphering mechanisms of LBSL pathology.

Keywords

LBSL; leukodystrophy; leukoencephalopathy; mitochondria; DARS2; tRNA synthetase

Introduction

Leukoencephalopathy with brain stem and spinal cord involvement and lactate elevation (LBSL) is a rare, autosomal recessive disorder characterized by slowly progressive spasticity, ataxia, proprioceptive deficits, and in some cases, cognitive decline. Most patients harbor compound heterozygous mutations in the *DARS2* gene (Tzoulis et al., 2012) which encodes mitochondrial aspartyl-tRNA synthetase (mt-AspRS), a ubiquitously expressed enzyme which charges tRNA molecules with cognate amino acids essential for mitochondrial protein translation. Diagnosis of LBSL includes identification of pyramidal, cerebellar, and dorsal column abnormalities on MRI, often presenting with increased lactate detected by proton-magnetic resonance spectroscopy (Scheper et al., 2007; van Berge et al., 2013). Age of onset and degree of disability vary widely with genotypic variation complicating a genotype-phenotype correlation (van Berge et al., 2014). With this said, more severe early infantile onset cases with seizures, microcephaly and global delay have also been reported (Sauter et al., 2015; Steenweg et al., 2012). Since the first descriptions of LBSL, human diseases have now been associated with each of the 19 mitochondrial tRNA synthetases, all presenting with diverse clinical symptoms (Sissler et al., 2017; Theisen et al., 2017).

Recapitulating *DARS2* deficiency and pathology in mouse or cell systems has proven difficult. Previous efforts to develop model animals have revealed that *Dars2* is essential for embryonic development, as a complete knock-out results in lethality around embryonic day 8.5, most likely due to the absence of proteins necessary for mitochondrial DNA maintenance (Dogan et al., 2014; Tyynismaa and Suomalainen, 2009) and attempts to recreate human mutations in the mouse have so far been unsuccessful. LBSL patient deficits are limited to the central nervous system (CNS) and thus CNS specific deletions of *DARS2* may best expose the roles of *DARS2* in the brain. Inducing *DARS2* mutations in various human cell types *in vitro* revealed neuronal-type cells to show the greatest deficit (van Berge et al., 2012) and further, selective deletion of *Dars2* from CamKIIα-expressing neurons in the mouse results in severe neurodegeneration and microglial activation, while selective oligodendrocyte Dars2 deletion produces a more mild phenotype (Aradjanski et al., 2017). In this study we conducted long-term detailed characterization of a similar mouse model describing their motor-behavioral profile in conjunction with *in vivo* Magnetic Resonance Imaging followed by post mortem histological studies and gene expression studies to elucidate the underlying disease pathophysiology.

Material and Methods

Mouse Breeding and Maintenance

Tissue-specific *Dars2* knock-out mice were generated using the Cre-LoxP system. LoxP-flanked *Dars2* mice (as described in Dogan et al., 2014) were mated with mice expressing cre-recombinase under the regulation of the CamKIIα promotor (The Jackson Laboratory stock no. 005359) to selectively knock-out *Dars2* expression in CamKIIα-expressing neurons (mutant mice). All experimental mice were bred in house and genotyped for presence of homozygous flox sites and cre by Transnetyx (Cordova, TN). All animal procedures were carried out in accordance with the *National Institutes of Health Guide for the Care and Use of Laboratory Animals* and were approved by the Institutional Animal Care and Use Committee of Johns Hopkins University.

Behavior

Behavioral assessments were performed in control (n = 12) and mutant (n = 12) mice. Assessment of open field behavior began on or around post-natal day (PND) 50 and continued bi-weekly until perfusion on or around PND 250. Open field (45 × 45 cm) activity over a 10-minute period was assessed using the Photobeam Activity System from San Diego Instruments in which distance traveled, time in center, and rearing activity were measured.

Magnetic Resonance Imaging

Six- and nine-month old control (6 month, n = 5; 9 month, n = 2) and mutant mice (6 month, n = 3; 9 month, n = 5) were anesthetized with isoflurane and imaged using a Bruker Biospec horizontal 11.7 T animal scanner (Bruker Corp., Billerica, MA) in the F.M. Kirby Research Center High-Field Preclinical MR Facility at the Kennedy Krieger Institute. Heart and respiratory rates were monitored throughout image acquisition. Following a localizer scan, T2-weighted images were acquired using the following parameters: echo time (TE)/ repetition time (TR) = 30/4600 ms, 2 signal averages, with a FOV of 20 × 20 mm^2, matrix size of 256 × 256, and a total of 45 slices of 0.5 mm thickness. Total scan time was approximately five minutes per animal. Images were reconstructed and analyzed using ROI Editor software by experimenters blinded to groups.

Histology and imaging

As pathology was evident at six months of age, for histological assessment, mice were anesthetized and transcardially perfused with saline and 4% paraformaldehyde at an early (5 months; control n = 4; mutant n = 6) and severe time point (9 months of age; behavioral mice). Brains and spinal cords were harvested, post-fixed overnight, cryoprotected, and stored at −80 °C until cryostat sectioning at 20 μm. For immunohistochemistry, sections were blocked (10% normal serum, 0.3% Triton-X in PBS) for 1 h at room temperature prior to overnight incubation with IBA1 (1:1000 in PBS; DAKO, Agilent, Santa Clara, CA) or CD68 primary (1:250 in PBS, conjugated Alexa Fluor® 647; Santa Cruz Biotechnology, Dallas, TX) at 4°C. On day 2, secondary incubation lasted 1 h at room temperature using goat anti-rabbit AlexaFluor 488 secondary (1:500 in PBS). Sections were rinsed, incubated with Hoescht dye (1:3000) for 3 minutes, rinsed, and coverslipped. Similarly, fluoromyelin

red (FMR; Thermo Fisher, Waltham, MA) was performed on adjacent sections according to manufacturer's instructions. Tissue was imaged using a Zeiss LSM 700 Confocal or a Zeiss Axio Imager M2 microscope operating AxioVision 4.8.2 (Zeiss; Oberkochen, Germany). Z-stacks of four 1 μm thick images were compressed and analyzed using FIJI (ImageJ 1.52h; National Institutes of Health, USA).

Electron Microscopy

A second cohort of control (n=4) and 3 mutant (n=3) mice were perfused for electron microscopy (EM) at nine months of age. Because myelin fixation has traditionally proven difficult to achieve at the ultrastructural level, a novel combination buffer system (involving reduced osmium; Langford and Coggeshall, 1980) was used here to achieve near perfect myelin preservation. Mice were perfused with a solution containing 2% glutaraldehyde, 2% paraformaldehyde (freshly prepared from EM grade prill), 50 mM sodium cacodylate, 50 mM phosphate (Sorenson's), 3 mM MgCl2, pH 7.2 at 1085 mOmols. Brains were then removed, and the corpus callosum was isolated and placed in fresh fixative overnight at 4 °C. The following steps were kept cold (4 °C) until the 70% ethanol step, then run at room temperature. Samples were rinsed in 75 mM cacodylate, 75 mM phosphate, 3.5% sucrose, 3mM MgCl2, pH 7.2 at 430 mOsmols for 45 min, microwaved (50% power, 10 sec. pulse-20 sec. pause-10 sec. pulse in a Pelco laboratory grade microwave model 3400), and post-fixed in 2% osmium tetroxide reduced with 1.6% potassium ferrocyanide in the same buffer without sucrose, then placed on ice in the dark for 2 hours. Samples were then rinsed in 100 mM maleate buffer with 3.5% sucrose pH 6.2, en-bloc stained for 1 hour with filtered 2% uranyl acetate in maleate sucrose buffer, pH 6.2. Following en-bloc staining, samples were dehydrated through a graded series of ethanol to 100%, transferred through propylene oxide, embedded in Eponate 12 (Pella) and cured at 60 °C for two days.

Sections were cut on a Reichert Ultracut E microtome with a Diatome Diamond knife (45 degree). 60 nm sections were picked up on formvar coated 1 × 2 mm copper slot grids and stained with methanolic uranyl acetate followed by lead citrate. Grids were viewed on a Hitachi 7600 TEM operating at 80 kV and digital images captured with an XR50 5 megapixel CCD by AMT.

RNAseq

To better understand the mechanisms contributing to the observed deficits, a third cohort of control (n=6) and mutant (n=7) male mice were saline perfused at 16 weeks old and cortices were dissected frozen and analyzed using RNAseq. This time point was selected as it just precedes both a behavioral phenotype and cellular/morphological changes in the cortex and may offer early insights into the pathogenic processes. RNA was isolated from tissue samples with a Qiagen RNeasy Lipid kit. RNA quality and concentration were assayed with a Fragment Analyzer instrument. RNA-seq libraries were prepared using the TruSeq Stranded mRNA Poly A (Unique Dual Index) RNA kit (Illumina, San Diego, CA). Libraries were sequenced on one lane of an Illumina HiSeq 4000 instrument. Alignment to the mouse transcriptome was performed with the STAR aligner (Dobin et al., 2013) and quantification of transcript abundances in units of Transcript Per Million (TPM) units was performed with MMSEQ (Turro et al., 2011). Differential expression analysis between the genotypes was

performed with MMDIFF (Turro et al., 2014). A threshold for confidence was set to exclude genes with fewer than 50 average reads, and resultant fold change of gene expression was determined relative to control littermates. Pathway analyses were completed using Ingenuity Pathway Analysis (IPA; Qiagen) version 46901286. Top pathways were visualized for expression differences and consistency among transcripts that were up- or down-regulated.

RNAseq data were validated with RT-PCR using a separate cohort of four control and four mutant mice. Male and female mice were aged at 9 months and showing signs of pathology. Cortices were again dissected frozen to look for upregulation and confirmation of highly changed genes detected by RNAseq. RNA was extracted using RNeasy isolation kits (Qiagen, Germantown, MD) and single stranded cDNA was generated using the High-Capacity cDNA Reverse Transcription Kit (Thermo Fisher). cDNA was diluted and expression of *Cst7* (forward `GGAGCTGTACTTGCCGAGC`; reverse `CATGGGTGTCAGAAGTTAGGC`), *Ctsc* (forward `CAACTGCACCTACCCTGATCT`; reverse `TAAAATGCCCGGAATTGCCCA`), *MhcII* (forward `AGCCCCATCACTGTGGAGT`; reverse `GATGCCGCTCAACATCTTGC`), *Iba1* (forward `ATCAACAAGCAATTCCTCGATGA`; reverse `CAGCATTCGCTTCAAGGACATA`), *Cd68* (forward `TGTCTGATCTTGCTAGGACCG`; reverse `GAGAGTAACGGCCTTTTTGTGA`), and *Ppia* forward `GAGCTGTTTGCAGACAAAGTTC`; reverse `CCCTGGCACATGAATCCTGG`) were measured using a BioRad CFX384 system. Results were quantified using the $2^{-\Delta\Delta CT}$ method, standardized to *Ppia* and normalized to control expression.

Data Analysis

Behavioral and histological analyses were analyzed by two-way ANOVA with genotype and time as factors. EM and rt-pcr results were averaged by group and compared by student's t-test. For RNAseq expression data, fold-change and significance were calculated relative to control expression using MMDIFF. Pathway significance was determined by IPA. Statistics were completed using SPSS version 25. Graphs are depicted as means ± standard error of the mean (SEM) and findings were considered significant when $p \leq 0.05$.

Results

CamKII-Dars2 KO mice show increased activity and brain atrophy by 6 months of age

Analysis of open field activity revealed a significant increase of overall activity in CamKII-*Dars2* KO mice compared to littermate controls (Figure 1A; main effect: genotype, $F_{1,212} = 207.35$, $p < 0.0001$; age, $F_{15,212} = 8.52$, $p < 0.0001$). Sidak's correction for multiple comparisons demonstrated significant differences between control and KO total distance traveled beginning at 22 weeks ($p < 0.05$) and continuing throughout the duration of testing. Rearing behavior was also increased in CamKII-*Dars2* KO mice (main effect of genotype, $F_{1,212} = 71.430$, $p < 0.0001$; data not shown); however, time in center of the open field was indifferent between groups. CamKII-*Dars2* KO mice showed significantly increased body mass until 22 weeks of life when they fail to maintain the same trajectory and begin to resemble littermate control mice (main effect of genotype, $F_{1,404} = 15.14$, $p < 0.001$; Figure 1B).

Brain area as assessed by high resolution T2 (Figure 2A) showed significant atrophy in CamkII-*Dars2* KO mice (main effect of genotype, $F_{1,11} = 9.64$, $p < 0.01$) beginning at six months of age and progressing by nine months of age (Figure 2B, C). At nine months, the third and lateral ventricles are markedly enlarged, with most tissue loss occurring in the hippocampus and cortex. Cerebellum appeared normal.

Histological analysis shows significant neuroinflammation

Measurements of cortical atrophy from histological sections were consistent with MRI data and showed cortical thickness reduction and ventricle enlargement in an age-dependent manner. Cortical thickness appeared normal at five months of age; however, as expected, CamkII-*Dars2* KO mice have approximately half the cortical thickness of their littermate controls at nine months of age (main effect of: genotype $F_{1,10} = 25.51$, $p < 0.0001$, age $F_{1,10} = 18.79$, $p < 0.0001$; post hoc nine-month control vs mutant, $p < 0.0001$; Figure 3A, B). Similar to changes to cortical thickness, corpus callosum thickness was reduced by nine months of age ($p = 0.08$; Figure 3C). In the cortex, the number of IBA1+ cells was significantly increased (main effect of genotype $F_{1,7} = 6.406$, $p < 0.05$; Figure 3D) and the mean area of these cells was reduced, suggesting fewer/shorter processes and an activated state (main effect of genotype $F_{1,7} = 8.081$, $p < 0.05$; post hoc nine month control vs mutant $p < 0.05$; Figure 3E). Consistent with neuroinflammation, IBA+ microglial cells in 9 mo old mutant mice show greater expression of CD68, a protein highly expressed in activated microglia (Figure 3F, G). Lastly, density of neurons with the hippocampus was markedly decreased as thinning of the pyramidal neurons of the CA1 and granule cells of the dentate gyrus is apparent. Within the cortex, neuronal loss is apparent throughout all cortical layers with nearly complete loss in cortical layer IV (Supplemental Figure 1), a loss occurring despite reports of a nonuniformed distribution of CamKIIα positive cells within mouse cortical layers (Wang et al., 2013).

Corpus callosum thickness is reduced but axons show increased mitochondrial number

Similar to reductions in cortical thickness, corpus callosum thickness at midline showed a similar pattern of reduction (Figure 3C; $p > 0.05$). Fluoromyelin red staining of corpus callosum in mice showed increased intensity of dye in mutant mice, suggesting increased density of myelin despite slight reductions in overall thickness ($p < 0.05$; Figure 4A, B). EM analysis of fibers within the corpus callosum (Figures 4C–F) showed increased myelin thickness (Figure 4G; $t(5) = 3.19$, $p < 0.05$) and increased axonal area (Figure 4H; $t(5) = 3.89$, $p < 0.05$) at nine months of age, resulting in no difference in g-ratio between control (0.73 ± 0.003 SEM) and mutant mice (0.74 ± 0.03 SEM). Interestingly, although mitochondrial cristae appeared normal and mitochondrial area did not differ between control and mutant groups (Figure 4I; $t(5) = 0.13$, $p > 0.05$), on average, there was a greater number of mitochondria per axon in mutant mice compared to littermate controls (Figure 4J; $t(5) = 5.71$, $p < 0.01$), suggesting an increase in mitochondrial biogenesis, likely as a compensatory mechanism to increased respiratory deficiency.

RNA-seq data confirms increased inflammatory profile in CamKII-Dars2 KO mice

To identify changes in gene expression that precede the appearance of neurological and behavioral deficits in CamKII-*Dars2* KO mice, we performed RNA-seq on cortex from

control and mutant mice at 16 weeks of age. A total of 20,997 genes were identified in control and mutant mice. Of those, roughly 10% (2,058 total transcripts) were significantly enriched in mutant mice relative to their expression in littermate controls after comparing group fold changes by t-test. Analysis of these enriched genes using IPA revealed several canonical pathways to be significantly altered (see supplemental tables for a full list of the affected canonical pathways, Table 1; diseases and functions, Table 2; upstream regulators, Table 3; KEGG Pathway map of Cellular Adhesion Molecules, Supplemental Figure 2). Of these, several themes of biological significance emerged, including canonical pathways of immune regulation (chemokine, *Il-1*, *Il-2*, *Il-3*, *Il-8*, B-cell receptor, and T-cell receptor signaling), regulation of translation (assembly of RNA polymerase II complexes, EIF2 signaling, and regulation of eIF4 and p70S6k signaling), cell signaling (netrin, neuregulin, mTOR, CREB, ERK5, ERK/MAPK, PPARa, and IGF-1 signaling), and cell stress pathways (ER Stress pathway, unfolded protein response, NRF2-mediated oxidative stress response, oxphos, ROS in macrophages, mitochondrial dysfunction pathways). These data were further confirmed and visualized by mapping the top differentially expressed genes using iDEP.90 (Figure 5; Ge, Son, and Yao 2018).

Investigation into cell stress pathways at this time point implicate activation of the integrated stress response (ISR), a gene signature previously implicated in conditional deletion of mt-aaRS (Agnew et al., 2018; Dogan et al., 2014; Wong et al., 2019). Transcripts significantly altered within our dataset include *Asns* 1.66 log2 fold change, $p = 0.02$; *Atf5* 1.39 log2FC, $p = 0.04$; *Chac1* 2.52 log2FC, $p < 0.01$; *Ddit3* 1.91 log2FC, $p = 0.01$; *Pck2* 2.07 log2FC, $p < 0.01$; *Sesn2* 2.13 log2FC, $p < 0.01$; *Shmt2* 2.62 log2FC, $p < 0.01$; *Trib3* 1.81 log2FC, $p = 0.02$; and Eif2ak1 2.79 log2FC, $p < 0.01$. Interestingly, transcripts related to respiratory chain complexes I (*Nduf* family) and IV (*Mt-co1*; *Cox* family) noted in previous models remain largely unchanged.

Finally, to better understand the underlying significance of the transcriptomic changes observed, we conducted the identical analysis on differentially expressed genes that were increased or decreased 2- or more fold. IPA analysis of this smaller subset confirms that the majority of these transcripts are involved in immune activation and regulation, with the top 5 altered canonical pathways being the complement system, acute phase response signaling, antigen presentation, T helper cell differentiation, and role of pattern recognition receptors. Among the transcripts involved in these pathways, the most abundantly changed with a 228-fold increase was Cystatin F (*Cst7*; log2 fold change of 7.284), and its major target, cathepsin C (*Ctsc*; 1.84 log2FC). Integrin alpha-X (*Itgax*; 6.17 log2FC), and interferon family genes (*Ifi44*, *Ifi27l2a*, *Ifit1*, *Ifit3*, and *Ifitm3*, increased 5.12-, 4.90-, 4.25-, 2.96-, and 2.83 log2FC, respectively) were among the next highly altered transcripts. *Cst7*, a protease inhibitor which plays a role in immune regulation in disease states, was followed up and examined in relation to close interactors, including *Rac2* (2.22 log2FC, $p = 0.03$), *Ptprc* (3.62 log2FC, $p = 0.01$), cathepsin S (*Ctss*, 1.87 log2FC, $p < 0.001$), and *Cebpa* (1.78 log2FC, $p = 0.04$), a known transcription factor controlling *Cst7* (Dautović et al., 2018).

RT-PCR expression of certain targets including *Cst7*, *Ctsc*, *MhcII*, *Iba1*, and *Cd68* were tested in a separate group of nine-month old mice. Results confirmed the findings from RNAseq and showed increased expression of each gene (Figure 6; *Cst7*, 9.92-fold increase,

$p < 0.01$; *Ctsc*, 2.92-fold increase, $p < 0.01$; *MhcII*, 3.46-fold increase, $p < 0.05$; *Iba1*, 2.43-fold increase, $p < 0.01$; *Cd68*, 3.94-fold increase, $p < 0.01$) confirming activation in the cortex both at early and late time-points.

Discussion

In mouse, the selective deletion of *Dars2* in CamKII neurons results in a severe and progressive phenotype which includes hyperactivity, concurrent atrophy of cortical tissues, and increased presence and activation of microglial cells. Previous work in a similar mouse model (models differ in generation of CamKIIα-Cre line; see Xu et al., 2000) show cortical and hippocampal morphological changes occur as early as 20 weeks of age (Aradjanski et al., 2017), with atrophy emanating from the second and third cortical layers and progressing to encompass much of the cortex and hippocampus by the time points assessed within our experiments. Furthermore, selective *Dars2* deletion from cardiac tissues results in impaired mitochondrial proteostasis and very early activation of the mitochondrial unfolded protein response (UPR^{mt}) (Dogan et al., 2014). These early cellular precursors indicate processes which could be causal for the progressive and severe dysfunction in the mouse model at the ages assessed herein. Interestingly, in our hands, cortical atrophy progressed similarly, condensing all cortical layers leaving layer IV largely absent. Corpus callosum thickness was also significantly reduced likely as a result of neuronal and axonal death, and although myelinated fibers appeared more dense, integrity of the myelin was normal. Examination of mitochondrion by EM during the peak of behavioral disruption and microglial activation reveals an increased number of these precisely regulated organelles in mutant mice and suggests compensatory mechanisms for energy production; however, in contrast also reveals healthy appearing cristae and microstructure indifferent from control mice.

Misalignment between the severity of phenotype, inflammatory activation, and normal mitochondrial appearance during peak dysfunction and the subtle mitochondrial impairments detected during disease early stages begged the examination of cortical gene expression at a timepoint preceding phenotype onset. Transcript analysis from the cortex of 16-week-old mutant mice indicates gene expression changes relevant to activity of *Atf4,* a transcription factor involved in the ISR, which has been reported to be induced in various models of mitochondrial dysfunction (Kasai et al., 2019; Quirós et al., 2017) including mouse models of mitochondrial aaRS deficiency (Agnew et al., 2018; Dogan et al., 2014). Concurrent with activation of the ISR was the activation of several inflammatory pathways, including the innate immune response, immune effector processes, and cytokine production and regulation. Cell stress pathways such as the ISR or the cGAS-cGAMP-STING pathway, which triggers innate immune activation upon detection of cytosolic DNA or DNA damage, are both potential mechanisms by which inflammatory activity may precede and contribute to neurodegeneration (Bader and Winklhofer, 2019; Li and Chen, 2018).

Interestingly, of the upregulated transcripts in CamKII-*Dars2* KO mice, Cystatin F (*Cst7* or *CysF*), a papain-like lysosomal cysteine proteinase inhibitor reportedly induced in the CNS during active demyelination or remyelination (Ma et al., 2011), shows an over 200-fold increase of expression in *Dars2* mutant mice prior to gross changes in brain morphology. This potent endogenous cysteine protease inhibitor is not normally expressed in the healthy

brain, but is greatly upregulated primarily in activated microglia in the diseased brain (Duan et al., 2018; Kos et al., 2018; Ma et al., 2011; Shimizu et al., 2017). Several recent studies point to the role of *Cst7* as a master regulator of immune activity and immune cell cytotoxicity through its interactions with cathepsins, namely cathepsin C (*Ctsc*), a lysosomal cysteine protease also shown to be linked to inflammatory regulation during demyelination (Dautović et al., 2018; Duan et al., 2018, 2012; Kos et al., 2018; Wisessmith et al., 2018).

Microglial expression of *Cst7* and overlap of these cells in areas of active demyelination/remyelination have been confirmed across several models, and indeed functional roles of the gene have been associated with white matter lesions in cerebral hypoperfusion mice (Duan et al., 2012), cuprizone-induced demyelinating mouse models (Liang et al., 2016), mouse models of multiple sclerosis (MS) (Ma et al., 2011; Shimizu et al., 2017; Wlodarczyk et al., 2017), and human MS patients (Hendrickx et al., 2017). Full deletion of *Cst7* in knock out mouse models has resulted in worsened demyelination following cuprizone administration (Liang et al., 2016) potentially due to lost immune regulation by cathepsin C. One known activator of *Cst7, C/ebp* α, is a transcription factor of the CCAAT enhancer binding protein family essential for the development and differentiation of myeloid cells (Dautović et al., 2018). Studies of *C/ebp* α show *Cst7* to play a role in myeloid differentiation, as expression levels change with differentiation status (Dautović et al., 2018); however, although upregulated nearly 3-fold, the implications of increased *C/ebp α* in our model are unclear.

Importantly, we observe a highly increased expression of *Ctsc* in CamKII-*Dars2* KO mice. Cathepsin C, present in healthy neurons, is increased during neuroinflammation and plays an integral role in the activity and regulation of T-lymphocytes (Kos et al., 2018; Stoka et al., 2016). Characteristic T cell-mediated neuroinflammation leading to demyelination, axonal loss, and brain atrophy in chronic neurodegeneration (such as MS) requires cognate antigen exposure likely through MHC class II expressing dendritic cells (Mundt et al., 2019; Schetters et al., 2018). Interactions of MHCII expressing microglial cells with infiltrating T cells have been demonstrated and implicated in neurodegeneration within Parkinson's, Alzheimer's, and EAE mouse models in addition to human Parkinson's and Alzheimer's post-mortem brain tissue (Schetters et al., 2018). Indeed, gene expression analysis demonstrates altered activation of several cell signaling and inflammatory pathways at 16 weeks of age in mice lacking *Dars2* in CamKII expressing neurons. Additionally, the most affected genes are predominantly involved in immune regulation including T cell activity, and antigen presentation. Interestingly, in addition to classical immune regulatory genes, *C/ebp* α, implicated as a regulator of *Cst7*, is also cited to be involved with inflammatory processing of the acute-phase response after injury or infection (Burgess-Beusse and Darlington, 1998; Walton et al., 1998). It is possible that deletion of *Dars2* in CamKII expressing neurons in our model may lead to disruptions of neuronal homeostasis, chronic activation of neighboring microglial cells, and progressively altered CNS-immune interactions.

Within cortical tissue of CamKII-*Dars2* KO mice, several transcripts relevant to *Atf4* activation were altered despite little disruption of other mitochondrial genes or evidence of morphological changes to mitochondria. *DARS2* plays an important role in the translation of mitochondrial proteins, however several studies have shown limited effects on respiratory

chain complexes and mitochondrial function as a result of *DARS2* mutations (Dogan et al., 2014; Scheper et al., 2007). Conditional deletion of *Dars2* in mouse heart and skeletal muscle has shown progressive decreases in steady state and activity of respiratory chain complexes at 6-weeks of age which are preceded by changes characteristic of endoplasmic reticulum (ER) stress responses (Dogan et al., 2014). In this same model, elevations of *Atf5*, a transcription factor that is translationally and transcriptionally upregulated during activation of the ISR, is detectable in knock-out mice as early as one week old (Dogan et al., 2014). Furthermore, Agnew et al (2018) report tissue specific complex I deficiency and *Atf5* activation along with activation of the ISR, independent of mt-UPR, in mice carrying homozygous hypomorphic mutations in *Wars2*. In agreement with both models, our RNAseq analyses of cortical mouse tissue shows a two-fold increase in *Atf5* expression, which regulates protein homeostasis. In contrast, no changes to other major ISR regulators *Ppp1r15a, Eif2ak4,* or *Eif2ak3* are detected, which may be reflective of time of assessment, disagreement between gene expression and protein activity, and/or other mechanisms.

Together, gene expression data along with neuropathological and behavioral evidence support a severe inflammatory mechanism underlying the observed cortical cell loss. At 16 weeks, decreased transcript expression of synaptic organization and signaling in mutant mice likely reflects the early neuronal dysfunction which precedes significant neuronal loss throughout the cerebral cortex. Inflammatory mechanisms and the activation of microglial cells are known contributors to axonal damage and myelin loss, often accompanied by an increase in GFAP positive astrocytes – a pattern well characterized in mouse experimental autoimmune encephalomyelitis (EAE) models (Cassiani-Ingoni et al., 2006). Although the pathology of EAE models is triggered by immune activation, deletion of *Dars2* from CamKII neurons in our mouse model may result in a similar sequela and Aradjanski et al (2017) show microglial activation and astrogliosis precedes loss of cortical and hippocampal neurons. Finally, while there is a lack of evidence of major mitochondrial dysfunction as assessed morphologically and through gene expression analysis at these time points, further assessments of mitochondria in the CamKII-*Dars2* KO mice are needed to more fully elucidate the role of *Dars2* on mitochondrial function and mitochondrial protein translational machinery. The slow-yet-progressive neurodegenerative pathways may be fueled by disrupted homeostasis and uncontrolled immune processes within the CNS with possible contributions from activated cell stress pathways. The interactions of this system in our model are likely complex, and indeed both direct activation of inflammatory factors by the ISR (Deng et al., 2004) as well as adaptive and innate inflammatory contributions to ISR activity have been noted (Scheu et al., 2006; Tauber and Parker, 2019)

Conclusions

To date, studies of LBSL describe case reports of brain pathology and corresponding symptomology, or patient-derived cell line function (*DARS2* production or splice efficiency). Mutation heterozygosity and overall lack of post-mortem tissue blur our ability to decipher variant contributions or effects on mixed cell populations. Further, as these reports have demonstrated, patient cells produce decreased but sufficient amounts of *DARS2* protein and mutations most commonly affect residues conserved amongst mammals only, leading some to suggest pathology of LBSL to stem from dysfunction of non-canonical

functions of the enzyme (Ognjenović and Simonović, 2017; Simons et al., 2015; van Berge et al., 2012; van Berge et al., 2014). Alternatively, the activation of cell stress pathways and the crosstalk with inflammatory systems may link with the reported episodic worsening of symptoms in some patients with LBSL following immune challenges. While it is recognized that conditional mouse models such as described here do not fully recapitulate the human condition, as *Dars2* deficiency is limited to hippocampal and cortical neurons, mechanisms triggered by this deficiency may be shared and may help to elucidate pathways contributing to the slow and progressive dysfunction. These models may still serve as viable testbeds for potential therapeutics while exploring similar endpoints in other cell-specific models and/or patient-derived cells.

Supplementary Material

Refer to Web version on PubMed Central for supplementary material.

Acknowledgements:

Research reported in the manuscript was funded by A Cure for Ellie (acureforellie.org), and by National Institute of Health (NINDS 5R01NS097511, NICHD U54HD079123, and the Office of the NIH Director S10OD016374). The authors thank Lauren LeBon, Katherine Martin, Carmela Sidrauski, and Margaret Roy at Calico Life Sciences LLC for RNAseq data, analysis, and consultation. Additional thanks to Karen Smith-Connor and Mary E Blue for histology consultation, Joseph Mertz for IPA consultation, and the Johns Hopkins School of Medicine Behavioral Core.

References

Agnew T, Goldsworthy M, Aguilar C, Morgan A, Simon M, Hilton H, Esapa C, Wu Y, Cater H, Bentley L, Scudamore C, Poulton J, Morten KJ, Thompson K, He L, Brown SDM, Taylor RW, Bowl MR, Cox RD, 2018 A Wars2 Mutant Mouse Model Displays OXPHOS Deficiencies and Activation of Tissue-Specific Stress Response Pathways. Cell Rep. 25, 3315–3328.e6. 10.1016/j.celrep.2018.11.080 [PubMed: 30566859]

Aradjanski M, Dogan SA, Lotter S, Wang S, Hermans S, Wibom R, Rugarli E, Trifunovic A, 2017 DARS2 protects against neuroinflammation and apoptotic neuronal loss, but is dispensable for myelin producing cells. Hum.Mol.Genet. 0, 1–9. 10.1093/hmg/ddx307 [PubMed: 27798112]

Bader V, Winklhofer KF, 2019 Mitochondria at the interface between neurodegeneration and neuroinflammation. Semin. Cell Dev. Biol. 10.1016/j.semcdb.2019.05.028

Burgess-Beusse BL, Darlington GJ, 1998 C/EBPa Is Critical for the Neonatal Acute-Phase Response to Inflammation. Mol Cell Biol 18, 7269–7277. 10.1128/MCB.18.12.7269 [PubMed: 9819413]

Cassiani-Ingoni R, Coksaygan T, Xue H, Reichert-Scrivner SA, Wiendl H, Rao MS, Magnus T, 2006 Cytoplasmic translocation of Olig2 in adult glial progenitors marks the generation of reactive astrocytes following autoimmune inflammation. Exp. Neurol. 201, 349–358. 10.1016/j.expneurol.2006.04.030 [PubMed: 16814281]

Dautović E, Perišić Nanut M, Softić A, Kos J, 2018 The transcription factor C/EBP α controls the role of cystatin F during the differentiation of monocytes to macrophages. Eur J Cell Biol 97, 463–473. 10.1016/j.ejcb.2018.07.002 [PubMed: 30033148]

Deng J, Lu PD, Zhang Y, Scheuner D, Kaufman RJ, Sonenberg N, Harding HP, Ron D, 2004 Translational Repression Mediates Activation of Nuclear Factor Kappa B by Phosphorylated Translation Initiation Factor 2. Mol. Cell. Biol. 24, 10161–10168. 10.1128/mcb.24.23.10161-10168.2004 [PubMed: 15542827]

Dobin A, Davis CA, Schlesinger F, Drenkow J, Zaleski C, Jha S, Batut P, Chaisson M, Gingeras TR, 2013 STAR: Ultrafast universal RNA-seq aligner. Bioinformatics 29, 15–21. 10.1093/bioinformatics/bts635 [PubMed: 23104886]

Dogan SA, Pujol C, Maiti P, Kukat A, Wang S, Hermans S, Senft K, Wibom R, Rugarli EI, Trifunovic A, 2014 Tissue-specific loss of DARS2 activates stress responses independently of respiratory chain deficiency in the heart. Cell Metab. 19, 458–469. 10.1016/j.cmet.2014.02.004 [PubMed: 24606902]

Duan W, Ran H, Zhou Z, He Q, Zheng J, 2012 Adenosine A2A Receptor Deficiency Up-Regulates Cystatin F Expression in White Matter Lesions Induced by Chronic Cerebral Hypoperfusion. PLoS One 7, 1–9. 10.1371/journal.pone.0052566

Duan W, Wang H, Fan Q, Chen L, Huang H, Ran H, 2018 Cystatin F involvement in adenosine A2Areceptor-mediated neuroinflammation in BV2 microglial cells. Sci. Rep. 8, 1–14. 10.1038/s41598-018-25031-5 [PubMed: 29311619]

Ge SX, Son EW, Yao R, 2018 iDEP: An integrated web application for differential expression and pathway analysis of RNA-Seq data. BMC Bioinformatics 19, 1–24. 10.1186/s12859-018-2486-6 [PubMed: 29291722]

Hendrickx DAE, Scheppingen J. Van, Poel M. Van Der, Huitinga I, 2017 Gene Expression Profiling of Multiple Sclerosis Pathology Identifies Early Patterns of Demyelination Surrounding Chronic Active Lesions. Front Immunol 8 10.3389/fimmu.2017.01810

Kasai S, Yamazaki H, Tanji K, Engler MJ, Matsumiya T, Itoh K, 2019 Role of the ISR-ATF4 pathway and its cross talk with Nrf2 in mitochondrial quality control. J. Clin. Biochem. Nutr. 64, 2016–2019. 10.3164/jcbn.18

Kos J, Perišić M, Mateja N, Jerica P, Esmeralda S, Anahid D, 2018 Cystatin F as a regulator of immune cell cytotoxicity. Cancer Immunol. Immunother. 67, 1931–1938. 10.1007/s00262-018-2165-5 [PubMed: 29748898]

Langford LA, Coggeshall RE, 1980 The use of potassium ferricyanide in neural fixation. Anat Rec 197, 297–303. 10.1002/ar.1091970304 [PubMed: 6776846]

Li T, Chen ZJ, 2018 The cGAS–cGAMP–STING pathway connects DNA damage to inflammation, senescence, and cancer. J. Exp. Med. 215, 1287–1299. 10.1084/jem.20180139 [PubMed: 29622565]

Liang J, Li N, Zhang Y, Hou C, Yang X, Shimizu T, Wang X, Ikenaka K, Fan K, Ma J, 2016 Disinhibition of Cathepsin C Caused by Cystatin F Deficiency Aggravates the Demyelination in a Cuprizone Model. Front. Mol. Neurosci. 9, 1–12. 10.3389/fnmol.2018.00115 [PubMed: 26834556]

Ma J, Tanaka KF, Shimizu T, Bernard CCA, Kakita A, Takahashi H, Pfeiffer SE, Ikenaka K, 2011 Microglial cystatin F expression is a sensitive indicator for ongoing demyelination with concurrent remyelination. J. Neurosci. Res. 89, 639–649. 10.1002/jnr.22567 [PubMed: 21344476]

Mundt S, Mrdjen D, Utz SG, Greter M, Schreiner B, Becher B, 2019 Conventional DCs sample and present myelin antigens in the healthy CNS and allow parenchymal T cell entry to initiate neuroinflammation. Sci Immunol 4 10.1126/sciimmunol.aau8380

Ognjenović J, Simonović M, 2017 Human aminoacyl-tRNA synthetases in diseases of the nervous system. RNA Biol. 0, 00–00. 10.1080/15476286.2017.1330245

Quirós PM, Prado MA, Zamboni N, D'Amico D, Williams RW, Finley D, Gygi SP, Auwerx J, 2017 Multi-omics analysis identifies ATF4 as a key regulator of the mitochondrial stress response in mammals. J. Cell Biol. 216, 2027–2045. 10.1083/jcb.201702058 [PubMed: 28566324]

Sauter C, Lorber B, Gaudry A, Karim L, Schwenzer H, Wien F, Roblin P, Florentz C, Sissler M, 2015 Neurodegenerative disease- associated mutants of a human mitochondrial aminoacyl-tRNA synthetase present individual molecular signatures. Sci Rep 1–13. 10.1038/srep17332

Scheper GC, van der Klok T, van Andel RJ, van Berkel CGM, Sissler M, Smet J, Muravina TI, Serkov SV, Uziel G, Bugiani M, Schiffmann R, Krägeloh-Mann I, Smeitink J. a M., Florentz C, Van Coster R, Pronk JC, van der Knaap MS, 2007 Mitochondrial aspartyl-tRNA synthetase deficiency causes leukoencephalopathy with brain stem and spinal cord involvement and lactate elevation. Nat. Genet. 39, 534–539. 10.1038/ng2013 [PubMed: 17384640]

Schetters STT, Gomez-Nicola D, Garcia-Vallejo JJ, Van Kooyk Y, 2018 Neuroinflammation: Microglia and T cells get ready to tango. Front. Immunol. 8 10.3389/fimmu.2017.01905

Scheu S, Stetson DB, Reinhardt RL, Leber JH, Mohrs M, Locksley RM, 2006 Activation of the integrated stress response during T helper cell differentiation. Nat. Immunol. 7, 644–651. 10.1038/ni1338 [PubMed: 16680145]

Shimizu T, Wisessmith W, Li J, Abe M, Sakimura K, Chetsawang B, Sahara Y, Tohyama K, Tanaka KF, Ikenaka K, 2017 The balance between cathepsin C and cystatin F controls remyelination in the brain of Plp1-overexpressing mouse, a chronic demyelinating disease model. Glia 65, 917–930. 10.1002/glia.23134 [PubMed: 28251676]

Simons C, Griffin LB, Helman G, Golas G, Pizzino A, Bloom M, Murphy JLP, Crawford J, Evans SH, Topper S, Whitehead MT, Schreiber JM, Chapman KA, Tifft C, Lu KB, Gamper H, Shigematsu M, Taft RJ, Antonellis A, Hou YM, Vanderver A, 2015 Loss-of-function alanyl-tRNA synthetase mutations cause an autosomal-recessive early-onset epileptic encephalopathy with persistent myelination defect. Am. J. Hum. Genet. 96, 675–681. 10.1016/j.ajhg.2015.02.012 [PubMed: 25817015]

Sissler M, González-Serrano LE, Westhof E, 2017 Recent Advances in Mitochondrial Aminoacyl-tRNA Synthetases and Disease. Trends Mol. Med. 23, 693–708. 10.1016/j.molmed.2017.06.002 [PubMed: 28716624]

Steenweg M, van Berge L, van Berkel C, de Coo I, Temple I, Brockman K, Mendonca C, Vojta S, Kolk A, Peck D, Carr L, Uziel G, Feigenbaum A, Blaser S, Scheper G, van der Knaap MS, 2012 Early-Onset LBSL: How severe does it get? Neuropediatrics 43, 332–338. [PubMed: 23065766]

Stoka V, Turk V, Turk B, 2016 Lysosomal cathepsins and their regulation in aging and neurodegeneration. Ageing Res. Rev. 32, 22–37. 10.1016/j.arr.2016.04.010 [PubMed: 27125852]

Tauber D, Parker R, 2019 15-Deoxy-Δ 12,14 -prostaglandin J2 promotes phosphorylation of eukaryotic initiation factor 2α and activates the integrated stress response. J. Biol. Chem. 294, 6344–6352. 10.1074/jbc.RA118.007138 [PubMed: 30723157]

Theisen BE, Rumyantseva A, Cohen JS, Alcaraz WA, Shinde DN, Tang S, Srivastava S, Pevsner J, Trifunovic A, Fatemi A, 2017 Deficiency of WARS2, encoding mitochondrial tryptophanyl tRNA synthetase, causes severe infantile onset leukoencephalopathy. Am. J. Med. Genet. Part A 2505–2510. 10.1002/ajmg.a.38339 [PubMed: 28650581]

Turro E, Astle WJ, Tavaré S, 2014 Flexible analysis of RNA-seq data using mixed effects models. Bioinformatics 30, 180–188. 10.1093/bioinformatics/btt624 [PubMed: 24281695]

Turro E, Su S-Y, Goncalves A, Coin L, Richardson S, Lewin A, 2011 Haplotype and isoform specific expression estimation using multi-mapping RNA-seq reads. Genome Biol. 12 10.1056/nejm199801293380611

Tyynismaa H, Suomalainen A, 2009 Mouse models of mitochondrial DNA defects and their relevance for human disease 10 10.1038/embor.2008.242

Tzoulis C, Tran GT, Gjerde IO, Aasly J, Neckelmann G, Rydland J, Varga V, Wadel-Andersen P, Bindoff LA, 2012 Leukoencephalopathy with brainstem and spinal cord involvement caused by a novel mutation in the DARS2 gene. J Neurol 259, 292–296. 10.1007/s00415-0116176-9 [PubMed: 21792730]

van Berge L, Dooves S, van Berkel CGM, Polder E, van der Knaap MS, Scheper GC, 2012 Leukoencephalopathy with brain stem and spinal cord involvement and lactate elevation is associated with cell-type-dependent splicing of mtAspRS mRNA. Biochem. J. 441, 955–962. 10.1042/BJ20110795 [PubMed: 22023289]

van Berge L, Hamilton EM, Linnankivi T, Uziel G, Steenweg ME, Isohanni P, Wolf NI, Krägeloh-Mann I, Brautaset NJ, Andrews PI, De Jong BA, Al Ghamdi M, Van Wieringen WN, Tannous BA, Hulleman E, Würdinger T, Van Berkel CGM, Polder E, Abbink TEM, Struys EA, Scheper GC, Van Der Knaap MS, 2014 Leukoencephalopathy with brainstem and spinal cord involvement and lactate elevation: Clinical and genetic characterization and target for therapy. Brain 137, 1019–1029. 10.1093/brain/awu026 [PubMed: 24566671]

van Berge L, Kevenaar J, Polder E, Gaudry A, Florentz C, Sissler M, van der Knaap MS, Scheper GC, 2013 Pathogenic mutations causing LBSL affect mitochondrial aspartyl-tRNA synthetase in diverse ways. Biochem. J. 450, 345–50. 10.1042/BJ20121564 [PubMed: 23216004]

Walton M, Saura J, Young D, MacGibbon G, Hansen W, Lawlor P, Sirimanne E, Gluckman P, Dragunow M, 1998 CCAAT-enhancer binding proteinα is expressed in activated microglial cells after brain injury. Mol. Brain Res. 61, 11–22. 10.1016/S0169-328X(98)00169-7 [PubMed: 9795105]

Wang X, Zhang C, Szabo G, Sun Q-Q, 2013 Distribution of CaMKIIa expression in the brain in vivo, studied by CaMKIIa-GFP mice. Brain Res 70, 646–656. 10.1002/ana.22528.Toll-like

Wisessmith W, Shimizu T, Li J, Abe M, Sakimura K, Chetsawang B, Tanaka KF, Suzumura A, Tohyama K, Ikenaka K, 2018 Cathepsin C Modulates Myelin Oligodendrocyte Glycoprotein-induced Experimental Autoimmune Encephalomyelitis. J. Neurochem. 1–13. 10.1111/jnc.14581

Wlodarczyk A, Holtman IR, Krueger M, Yogev N, Bruttger J, Khorooshi R, BenmamarBadel A, de BoerBergsma JJ, Martin NA, Karram K, Kramer I, Boddeke EW, Waisman A, Eggen BJ, Owens T, 2017 A novel microglial subset plays a key role in myelinogenesis in developing brain. EMBO J. 36, e201696056. 10.15252/embj.201696056

Wong YL, LeBon L, Basso AM, Kohlhaas KL, Nikkel AL, Robb HM, Donnelly-Roberts DL, Prakash J, Swensen AM, Rubinstein ND, Krishnan S, McAllister FE, Haste NV, O'Brien JJ, Roy M, Ireland A, Frost JM, Shi L, Riedmaier S, Martin K, Dart MJ, Sidrauski C, 2019 eIF2B activator prevents neurological defects caused by a chronic integrated stress response. Elife 8, 1–31. 10.7554/elife.42940

Xu B, Zang K, Ruff NL, Zhang YA, McConnell SK, Stryker MP, Reichardt LF, 2000 Cortical Degeneration in the Absence of Neurotrophin Signaling. Neuron 26, 233–245. 10.1016/s0896-6273(00)81153-8 [PubMed: 10798407]

Highlights:

- Neuronal deletion of Dars2 in mice results in a slow and progressive neurodegeneration
- Dars2 induced degeneration is preceded by activation of several immune pathways
- Neuronal Dars2 deletion in mice may be a useful model in which to test therapeutics targeting the pediatric leukodystrophy, LBSL

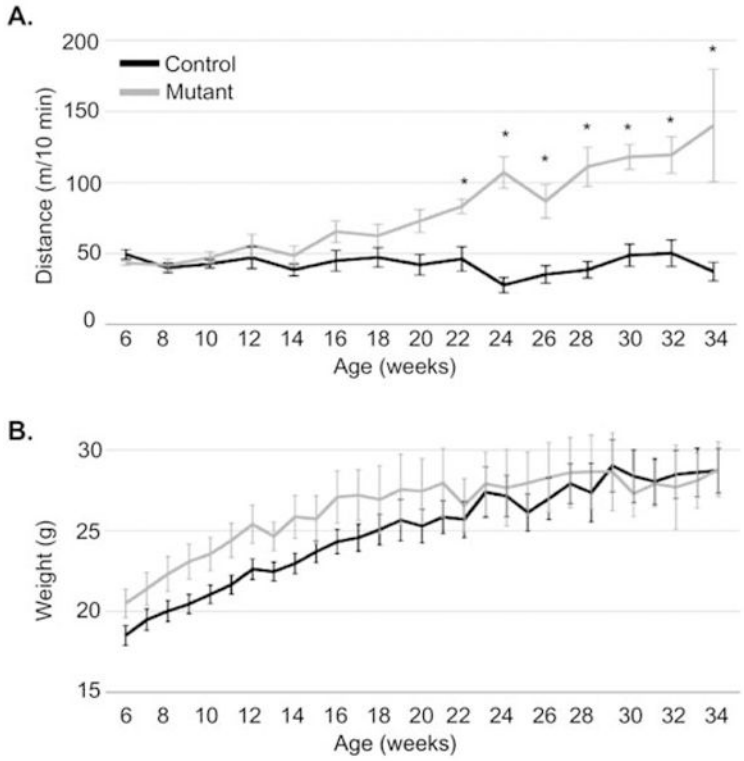

Figure 1:

(A) Control and CamKII-*Dars2* (mutant mice; n = 12 each group) were assessed in a 10-minute open-field every two weeks beginning at PND50. By 22 weeks of age, mutant mice show increased activity over 10 minutes and this pattern continues until testing was ceased at 34 weeks ($p < 0.05$). (B) Control and mutant body mass was measured every week beginning at 8 weeks of age and CamKII-*Dars2* mice show increased body mass compared to control mice for most of life (main effect of genotype, $p < 0.05$).

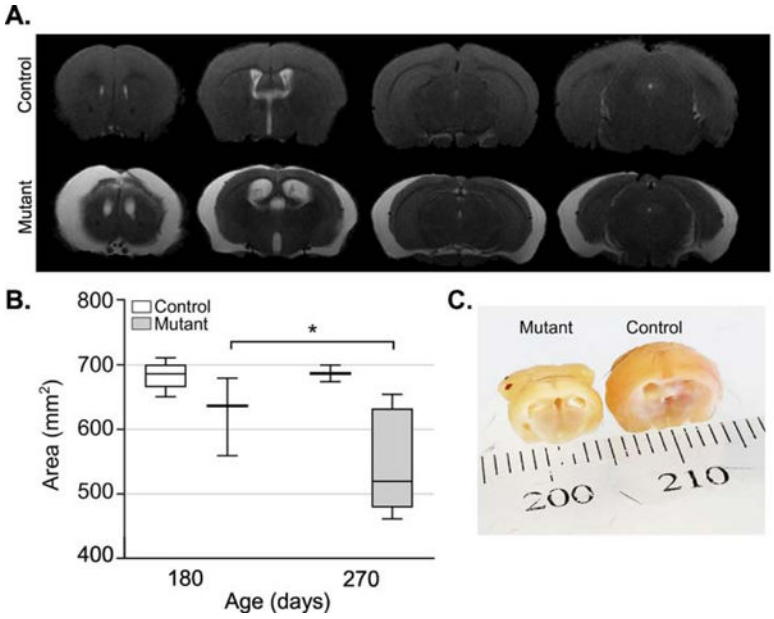

Figure 2:

(A) T2 weighted MRIs were taken of a subset of control and CamKII-*Dars2* mice at approximately six and nine months of age (control 6 month n = 5, 9 month, n = 2; mutant mice 6 month n = 3, 9 month n = 5). (B) Quantification of brain area reveals reductions of total area by six months of age which progresses by nine months of age (main effect of genotype, $p < 0.05$). (C) Photograph images of saline perfused brains are shown.

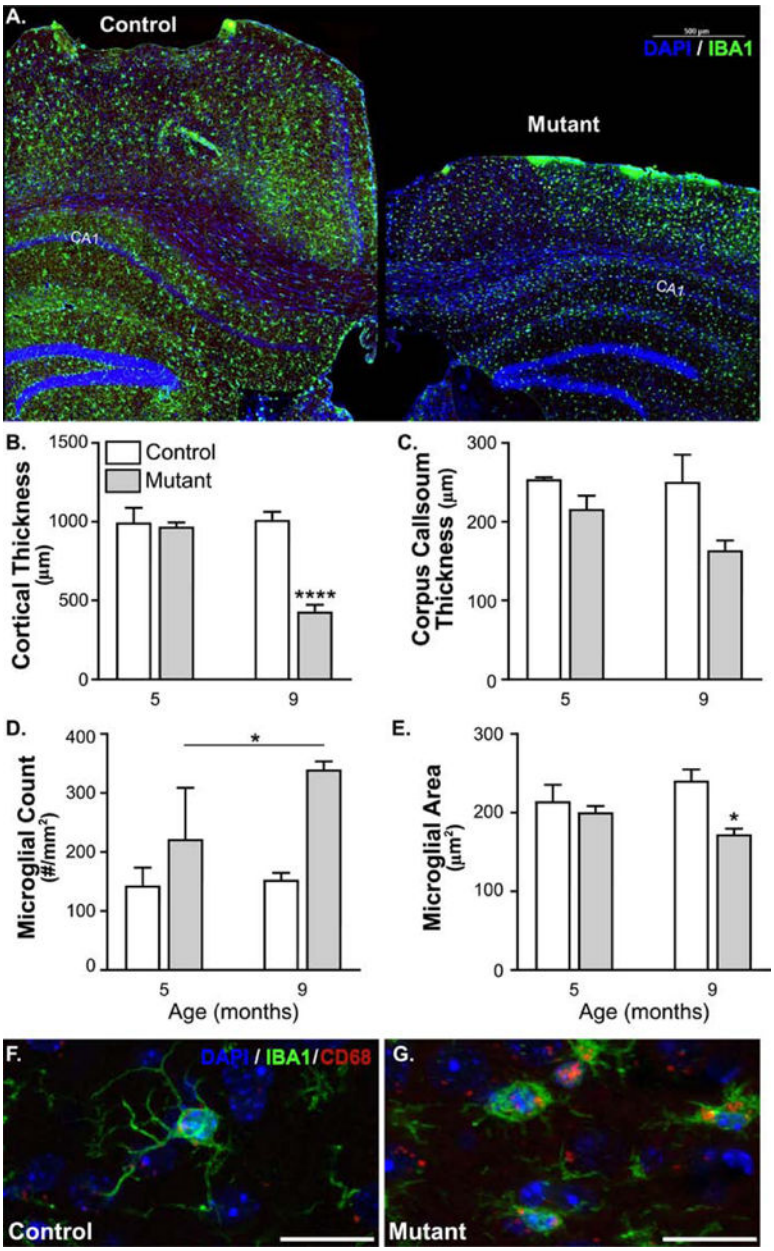

Figure 3:

(A) Histological staining of control and CamKII-*Dars2* (mutant) mice are shown with microglial cells stained with IBA1 (green) and nuclei with DAPI (blue). (B) Quantification of cortical thickness reveals significant reductions of midline thickness at nine months of age ($p < 0.05$). (C) Corpus callosum thickness also shows reductions by nine months of age (main effect of genotype; $p = 0.08$). (D) Count of IBA1+ microglial cells within the cortex shows upregulations at both five and nine months of age (main effect of age, $p < 0.05$). (E) The average area of individual microglial cells is reduced by nine months of age, signifying reduced processes and an activated state ($p < 0.05$). (F) Histological staining of control and mutant (G) IBA1+ microglia (green) stained with CD68 (red), a marker of microglial activation. Histology was assessed in 9 month old mice from behavior study (n = 12 for

each); 5 month old control (n = 4) and mutant (n = 6 mice) were added for comparison. Scale bar indicates 20 μm.

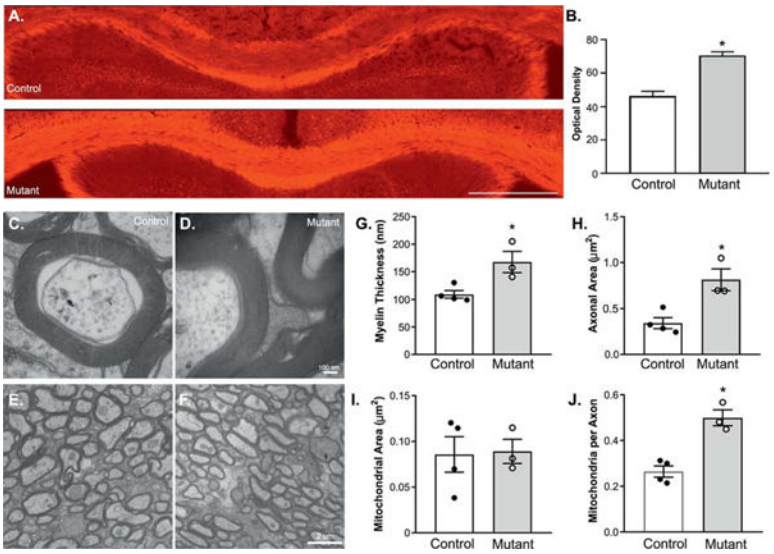

Figure 4:

(A) Fluromyelin Red staining of control and mutant corpus callosum shows more dense myelin in mutant samples; quantification in B. Scale bar represents 500 μm. Electron microscopy of control (C,E; n = 4) and CamKII-*Dars2* (D,F; mutant, n = 3) mice was done at nine months of age when significant behavioral and morphological changes are evident. Quantification within the corpus callosum shows increased myelin thickness in mutant mice (G; $p < 0.05$) as well as increased axonal area (H; $p < 0.05$). Although mitochondrial area was not different (I; $p > 0.05$), the average number of mitochondria per axon were increased in mutant mice compared to littermate controls (J; $p < 0.05$).

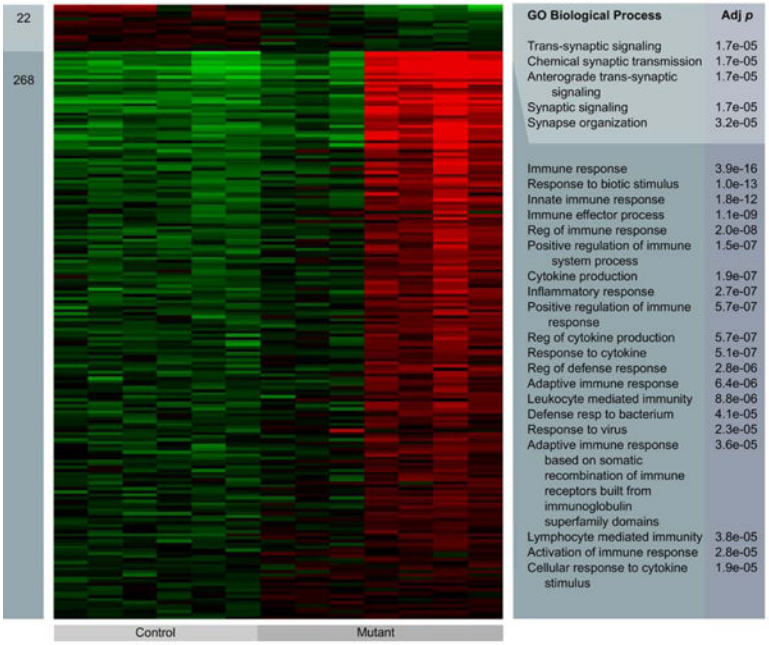

Figure 5:

Evaluation of differentially expressed genes show numerous altered pathways in the GO biological process domain GO terms and their associated adjusted *p*-value are shown.

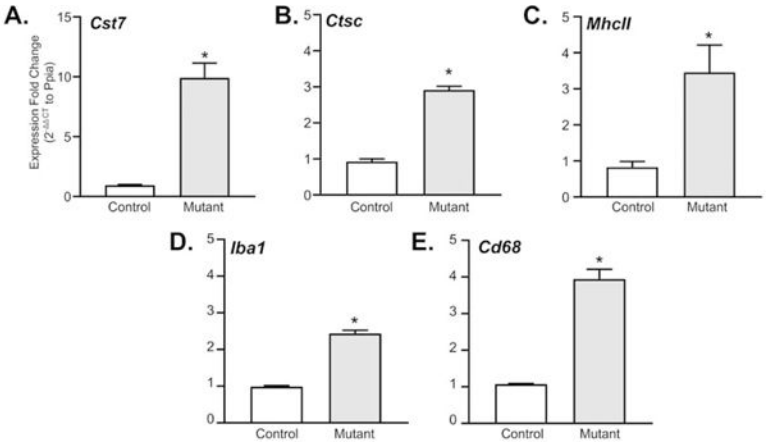

Figure 6:

Upregulated genes as measured by RNAseq were confirmed in a separate cohort of 9-month old mice using RT-PCR (n = 4 each group). At this time point, increases were confirmed for *Cst7* (A; 9.92-fold increase, $p < 0.01$), *Ctsc* (B; 2.92-fold increase, $p < 0.01$). *MhcII* (C; 3.46-fold increase, $p < 0.05$), *Iba1* (D; 2.43-fold increase, $p < 0.01$) and *Cd68* (E; 3.94-fold increase, $p < 0.01$).